INTERNATIONAL JOURNAL FOR NUMERICAL METHODS IN FLUIDS, VOL. 16, 133–152 (1993)

ON THE ACCURATE PREDICTION OF THE WALL-NORMAL VELOCITY IN COMPRESSIBLE BOUNDARY-LAYER FLOW*

C. DAVID PRUETT

Analytical Services and Materials, Inc., 107 Research Drive, Hampton, Virginia 23666, U.S.A.

SUMMARY

We consider a problem which arises in the numerical solution of the compressible two-dimensional or axisymmetric boundary-layer equations. Numerical methods for the compressible boundary-layer equations are facilitated by transformation from the physical (x, y) plane to a computational (ξ, η) plane in which the evolution of the flow is 'slow' in the time-like ξ direction. The commonly used Levy–Lees transformation results in a computationally well-behaved problem, but it complicates interpretation of the solution in physical space. Specifically, the transformation is inherently non-linear, and the physical wall-normal velocity is transformed out of the problem and is not readily recovered. Conventional methods extract the wall-normal velocity in physical space from the continuity equation, using finite-difference techniques and interpolation procedures. The present spectrally accurate method extracts the wall-normal velocity directly from the transformation itself, without interpolation, leaving the continuity equation free as a check on the quality of the solution. The present method for recovering wall-normal velocity, when used in conjunction with a highly accurate spectral collocation method for solving the compressible boundary-layer equations, results in a discrete solution which satisfies the continuity equation nearly to machine precision. As demonstration of the utility of the method, the boundary layers of three prototypical high-speed flows are investigated and compared: the flat plate, the hollow cylinder, and the cone. An important implication for classical linear stability theory is also briefly discussed.

KEY WORDS Boundary-layer equations Spectral collocation methods Compressible flow Wall-normal velocity

1. INTRODUCTION

In modern aerodynamics, the boundary-layer approximation is an invaluable tool of widespread applicability. Although it is still beyond the capability of existing supercomputers to solve the compressible Navier–Stokes equations for complete aerodynamic configurations, it is commonplace for engineering purposes to patch inviscid 'outer' solutions to the Euler equations with 'inner' solutions to the boundary-layer equations to obtain realistic lift and drag estimates. A different application, and the motivation for this work, lies in the area of stability and transition, for which solutions to the boundary-layer equations provide the mean velocity and temperature distributions necessary for linear and non-linear stability analyses. In this latter context, accuracy is quite important, since, in general, the stability of wall-bounded flow is extremely sensitive to variations in the mean.

* Research funded by the Theoretical Flow Physics Branch of the Fluid Mechanics Division, NASA Langley Research Center, under contract NASI-18599.

0271–2091/93/020133–20$15.00

Received 2 January 1992
Revised 4 August 1992

The boundary-layer equations define an Initial-Boundary-Value Problem (IBVP) in which the streamwise spatial co-ordinate is time-like. The solution is obtained by streamwise marching procedures. The equations are extraordinarily 'stiff', particularly for high-speed compressible flow. Consequently, only implicit marching techniques have met with practical success (for example, see References 1 or 2). Depending on the geometry of the flow, the time-like derivative may either enhance or undermine the diagonal dominance of the Jacobian used in the iteration procedure. To facilitate the numerical solution it is customary to transform the boundary-layer equations from physical (x, y) space to a computational (ξ, η) space in which the time-like derivative has 'nice' properties. In the ideal situation, a similarity solution exists, and the time-like derivative vanishes identically with the proper similarity transformation. Similarity solutions exist, however, only for a limited class of flows (e.g. flow over a flat plate in the absence of a streamwise pressure gradient). For non-similar flows, it is desirable that the time-like evolution in the transform plane be 'slow', and that the time-like derivative contribute to diagonal dominance of the Jacobian.

One transformation which exhibits these traits for a wide class of boundary-layer flows is that known commonly as the Levy–Lees transformation.[3]* Although the Levy–Lees transformation results in a computationally well-behaved problem, it complicates interpretation of the results in physical space, relative to the more straightforward transformations used for specialized applications by Duck[4] and by Pruett and Streett.[2] First, it is inherently non-linear, an additional reason why fully implicit methods are necessary. Second, the physical v-velocity is transformed out of the computational problem and is not easily recovered. For some applications, this is not of major concern. For example, classical linear stability analyses, which invoke the parallel-flow approximation, disregard the wall-normal velocity. It is now recognized, however, that the non-parallel effects on the stability of a high-speed flow can be significant,[5] and methods are being adapted and developed to treat non-parallelism. Among these are Spatial Direct Numerical Simulation (SDNS),[6] Multiple-Scale analyses (MS),[7,8] and a recent scheme based on the Parabolized Stability Equations (PSE).[9,10] Each requires accurate determination of wall-normal velocity, and the MS and PSE methods require its gradient as well. The quality (smoothness) of the solution is of particular importance whenever the application requires differentiated velocities.

Conventional methods exploit finite-different techniques and obtain the wall-normal velocity from the continuity equation.[11] The method presented here, designed as a companion to the spectral collocation method for the Compressible Boundary-Layer Equations (CBLE) developed by Pruett and Streett,[2] enjoys two major advantages over conventional approaches. First, the wall-normal velocity is computed to spectral accuracy. Second, the wall-normal velocity is extracted directly from the co-ordinate transformation, leaving the continuity equation available as a check on the quality of the solution. Using the method of Pruett and Streett[2] for the CBLE, and the present method to extract wall-normal velocity, we obtain a discrete solution which satisfies the continuity equation nearly to machine precision. Moreover, we obtain second derivatives of temperature and velocity distributions which are smooth to at least seven decimal places.

At the heart of the present method lies the non-trivial evaluation of the quantity η_x. In Section 2 the governing equations and non-dimensionalization are discussed, and the Levy–Lees transformation is defined. Section 3 details the numerical method, focusing on two independent derivations for η_x, both of which lead to relatively complicated expressions. In Section 4, in which

* White,[3] however, refers to this as the Illingworth–Levy–Lees–Dorodnitsyn–Probstein–Elliot transformation, mentioning also the contribution of Mangler.

we validate the method, both derivations of η_x are shown to give virtually identical numerical results. Section 5 provides an application of the method whereby the high-speed boundary layers of a flat plate, a hollow cylinder and a sharp cone are compared, with particular attention to their respective wall-normal velocity distributions. An important implication regarding the linear stability of the flow along a cone is also discussed. Finally, brief concluding remarks are offered in Section 6.

2. GOVERNING EQUATIONS

We consider the compressible, laminar boundary-layer flow along a two-dimensional or axisymmetric body at zero angle of incidence. Let x be the arc length along the body measured from the stagnation point, let y be the wall-normal co-ordinate, and let $r=r_0+y\cos\phi$ be the radial co-ordinate from the axis of revolution, as shown in Figure 1, where $r_0(x)$ is the body radius and $\phi(x)$ is the angle formed by the surface tangent and the axis of revolution. If u and v are the dimensionless velocity components in the x and y directions, respectively, and T, ρ and μ are, respectively, the dimensionless temperature, density and viscosity, then the flow is governed by[1]

$$\frac{\partial V}{\partial \eta}+2\xi\frac{\partial F}{\partial \xi}+F=0, \tag{1a}$$

$$2\xi F\frac{\partial F}{\partial \xi}+V\frac{\partial F}{\partial \eta}-\frac{\partial}{\partial \eta}\left[t^{2j}\frac{\tilde{\mu}}{\theta}\frac{\partial F}{\partial \eta}\right]+\frac{2\xi}{u_e}\frac{\mathrm{d}u_e}{\mathrm{d}\xi}(F^2-\theta)=0, \tag{1b}$$

$$2\xi F\frac{\partial \theta}{\partial \xi}+V\frac{\partial \theta}{\partial \eta}-\frac{1}{Pr}\frac{\partial}{\partial \eta}\left[t^{2j}\frac{\tilde{\mu}}{\theta}\frac{\partial \theta}{\partial \eta}\right]-(\gamma-1)M_e^2t^{2j}\frac{\tilde{\mu}}{\theta}\left[\frac{\partial F}{\partial \eta}\right]^2=0, \tag{1c}$$

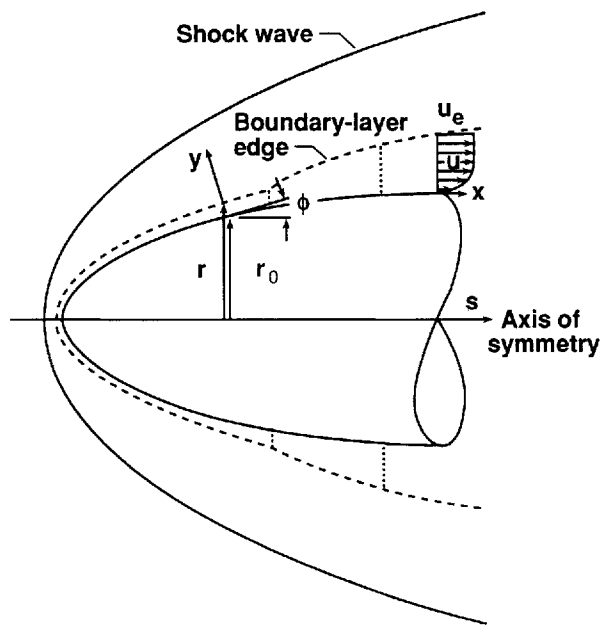

Figure 1. Body-fitted co-ordinate system

where we have exploited the following transformations:

$$F=\frac{u}{u_e}, \qquad \theta=\frac{T}{T_e}=\frac{\rho_e}{\rho}, \qquad \tilde{\mu}=\frac{\mu}{\mu_e}, \tag{2a}$$

$$V=\frac{2\xi}{\rho_e u_e \mu_e r_0^{2j}}\left[F\frac{\partial\eta}{\partial x}+\frac{\sqrt{Re}\,\rho v r^j}{\sqrt{2\xi}}\right], \tag{2b}$$

$$\xi(x)=\int_0^x \rho_e u_e \mu_e r_0^{2j}\,\mathrm{d}\bar{x}, \tag{2c}$$

$$\eta(x,y)=\frac{\sqrt{Re}\,\rho_e u_e r_0^j}{\sqrt{2\xi}}\int_0^y t^j\frac{\rho}{\rho_e}\,\mathrm{d}\bar{y}, \tag{2d}$$

$$t=\left[\frac{r}{r_0}\right]^j=\begin{cases}1 & (j=0),\\ 1+\dfrac{y\cos\phi}{r_0} & (j=1).\end{cases} \tag{2e}$$

In equations (1) and (2), the subscripts 'e' designate values at the boundary-layer edge, which vary only in x, and which are assumed to be known, for example, from the solution of the Euler equations. Details of the derivation of equations (1) can be found in Reference 1. Briefly, equations (1) follow from the compressible Navier–Stokes equations via the boundary-layer approximation,[3] and describe, respectively, conservation of mass, streamwise momentum and energy. For $j=0$ and $j=1$, equations (1) describe, respectively, laminar two-dimensional and axisymmetric boundary-layer flow.

Following Reference 1, lengths, velocities and density in equations (1) and (2) have been normalized by the arbitrary reference values L^*, u_r^* and ρ_r^*, respectively. The reference temperature is taken to be $T_r^*=u_r^{*2}/C_p^*$, where C_p^* is the specific heat at constant pressure, and the reference viscosity $\mu_r^*=\mu^*(T_r^*)$. Throughout this paper, dimensional quantities are denoted by an asterisk.

The parameters which arise in equations (1) and (2) as a result of non-dimensionalization are the Reynolds number Re, the Prandtl number Pr and the ratio of specific heats γ. Specifically, these are defined as

$$Re=\frac{\rho_r^* u_r^* L^*}{\mu_r^*}, \qquad Pr=\frac{C_p^*\mu_r^*}{\kappa_r^*}, \qquad \gamma=\frac{C_p^*}{C_v^*}, \tag{3}$$

where C_v^* is the specific heat at constant volume and κ_r^* is the (reference) value of the thermal conductivity at the reference temperature, T_r^*. Here, we have assumed the fluid to be an ideal gas. For ideal gases, C_p^* and C_v^* are constant, and the ideal gas constant $R_g^*=C_p^*-C_v^*$. We note that Mach number appears not as a true parameter but as edge data, where $M_e=u_e^*/\sqrt{(\gamma R_g^* T_e^*)}$. Finally, equations (1) are closed by assuming $\tilde{\mu}(\theta)$ to vary according to Sutherland's law, namely

$$\tilde{\mu}=\frac{\theta^{3/2}(1+C_1)}{\theta+C_1}, \qquad C_1=\frac{198{\cdot}6^\circ\mathrm{R}}{T_e^*}.$$

Transformation (2c, d), from the physical space (x, y) to be computational space (ξ, η), is known as the Levy Lees transformation and is commonly used to facilitate the numerical solution of the boundary-layer equations. In the experience of the author, the Levy–Lees and associated transformations (2) are essential for the accurate numerical solution of a non-similar boundary-layer flow in which the streamwise velocity profile becomes 'thinner' as one proceeds down-

stream, e.g. boundary-layer flow along a sharp cone. For example, when the spectral collocation method of Pruett and Streett[2] using the straightforward transformation of Duck[4] is applied for the case of $M_e = 6{\cdot}8$ flow over a 7° half-angle cone, the Jacobian of the iteration procedure becomes very ill-conditioned. For a highly resolved grid, the condition number can be $O(10^{15})$ or larger. In contrast, when transformation (2) is incorporated into the method, the condition number is typically $O(10^8)$. In the former case, the extreme ill-conditioning prevents full convergence of the iteration procedure, resulting in an excessively noisy solution.

The utility of the Levy–Lees transformation, therefore, is that it results in a well-conditioned governing system for an entire class of axisymmetric or two-dimensional boundary-layer flows. It is inherently non-linear, however, because the transformation depends upon the solution itself. Since solution methods for the boundary-layer equations are implicit and, hence, iterative, the non-linearity of the transformation is not a major problem. The difficulty with transformations (2), however, with which we deal in the next section, is that equation (2b) 'buries' the wall-normal velocity.

2. NUMERICAL METHODS

From equation (2b) one obtains the following expression for the wall-normal velocity v in the transform (ξ, η) plane:

$$v(\xi, \eta) = \frac{\sqrt{2\xi}}{\sqrt{Re}} \frac{\theta}{r^j} \left[\frac{u_e \mu_e r_0^{2j} V}{2\xi} - \frac{F}{\rho_e} \frac{\partial \eta}{\partial x} \right]. \tag{4}$$

Provided the quantities on the right-hand side of equation (4) are known, the determination of v is trivial. The difficulty with equation (4), however, is that a closed-form expression for η_x is not readily available, nor is its form simple. Because of the complicated nature of η_x, and because we are unaware of any previously existing derivation for the general case, we present two independent derivations which we then use for (numerical) cross-validation. In the first method, η_x is obtained from the Jacobians of transformation (2c, d) and its inverse. In the second method, η_x is shown to be the solution of a linear Fredholm integral equation whose coefficients are constructed from information available from the solution of equations (1). For both methods, the computational effort required to evaluate η_x (and, subsequently, v) is insignificant relative to that required to solve boundary-layer equations (1). For brevity, we have omitted most of the details of these somewhat tedious derivations. The interested reader can find the complete derivations in Reference 12.

Before proceeding, we note that the evaluation of t in the boundary-layer equations (1), and both methods for extracting v, make use of the inverse transformation corresponding to equations (2c, d). Whereas the inverse of (2c) is straightforward and is omitted, the inverse of (2d) requires the solution of a quadratic equation which results in the following:

$$y(\xi, \eta) = \begin{cases} \dfrac{\sqrt{2\xi}}{\sqrt{Re}\,\rho_e u_e} \displaystyle\int_0^\eta \theta \, d\bar{\eta} \equiv y_{2D} & (j=0) \\ \dfrac{2y_{2D}}{r_0(1+\sqrt{1+C})} & (j=1) \end{cases} \tag{5a}$$

where

$$C(\xi, \eta) \equiv \frac{2 \cos \phi \, y_{2D}}{r_0^2}. \tag{5b}$$

Note that the planar ($j=0$) expression must be evaluated to obtain y_{2D} prior to evaluation of the axisymmetric ($j=1$) expression,

Method 1

From the Levy–Lees transformation (2c, d) we obtain

$$\frac{\partial \eta}{\partial x}=-\frac{\partial \eta}{\partial y}\frac{\partial y}{\partial \xi}\frac{d\xi}{dx}. \tag{6}$$

To derive equation (6), we have made use of the fact that the product of the Jacobians of the transformation and its inverse must yield the 2×2 identity matrix. Two of the factors necessary to evaluate equation (6) are easily obtained from equations (2c, d) namely

$$\frac{d\xi}{dx}=\rho_e u_e \mu_e r_0^{2j}, \tag{7a}$$

$$\frac{\partial y}{\partial \eta}=\frac{\sqrt{2\xi}\theta}{\sqrt{Re}\,\rho_e u_e r^j}. \tag{7b}$$

The remaining factor, y_ξ, is complicated. After straightforward, though tedious, differentiation of equation (5) with respect to ξ, including the use of Leibnitz' rule to differentiate beneath the integral sign, we obtain

$$\frac{\partial y}{\partial \xi}(\xi,\eta)=\begin{cases}\left[\dfrac{1}{2\xi}-\dfrac{1}{\rho_e}\dfrac{d\rho_e}{d\xi}-\dfrac{1}{u_e}\dfrac{du_e}{d\xi}\right]y_{2D}+\dfrac{\sqrt{2\xi}}{\sqrt{Re}\,\rho_e u_e}\displaystyle\int_0^\eta \frac{\partial\theta}{\partial\xi}\,d\bar\eta\equiv\frac{\partial y_{2D}}{\partial\xi} & (j=0),\\ \left[\dfrac{1}{r_0}\dfrac{dr_0}{d\xi}+\tan\phi\dfrac{d\phi}{d\xi}\right]y-\dfrac{1}{r_0}\left[\dfrac{2}{r_0}\dfrac{dr_0}{d\xi}+\tan\phi\dfrac{d\phi}{d\xi}\right]\dfrac{y_{2D}}{\sqrt{1+C}}+\dfrac{1}{r_0\sqrt{1+C}}\dfrac{\partial y_{2D}}{\partial\xi} & (j=1).\end{cases} \tag{8}$$

As in the case of equation (5), one must evaluate the planar ($j=0$) expression prior to the axisymmetric ($j=1$) expression. The wall-normal velocity v follows immediately from equations (4) and (6)–(8).

We defer discussion of the procedure for evaluating the integrals in equations (5) and (8) until after the presentation of method 2.

Method 2

In this method, we differentiate equation (2d) implicitly with respect to x to obtain the following expression:

$$\begin{aligned}\frac{\partial\eta}{\partial x}(\xi,\eta)=&\left[\frac{1}{\rho_e}\frac{d\rho_e}{dx}+\frac{1}{u_e}\frac{du_e}{dx}-\frac{1}{2\xi}\frac{d\xi}{dx}-j\tan\phi\frac{d\phi}{dx}\right]\eta\\&+j\left[\tan\phi\frac{d\phi}{dx}+\frac{1}{r_0}\frac{dr_0}{dx}\right]\int_0^\eta\frac{1}{t}\,d\bar\eta-\frac{d\xi}{dx}\int_0^\eta\frac{1}{\theta}\frac{\partial\theta}{\partial\xi}\,d\bar\eta-\int_0^\eta\frac{1}{\theta}\frac{\partial\theta}{\partial\eta}\frac{\partial\eta}{\partial x}\,d\bar\eta.\end{aligned} \tag{9}$$

The derivation of equation (9) is somewhat involved, requiring the use of the chain rule to evaluate $\partial\theta/\partial x$, Leibnitz' rule to differentiate under integral signs, and the following integral transformation:

$$\int_0^y h(\bar y)\,d\bar y=\int_0^\eta h(\bar\eta)\frac{\partial y}{\partial\eta}\,d\bar\eta, \tag{10}$$

where h is an arbitrary function of η, and where $\partial y/\partial\eta$ is given in equation (7b). Complete details can be found in Reference 12.

Expression (9) is a linear Fredholm integral equation of the form

$$q(\xi,\eta)=\int_0^\eta w(\xi,\bar{\eta})q\,(\xi,\bar{\eta})\mathrm{d}\bar{\eta}+p(\xi,\eta),$$

where

$$q(\xi,\eta)=\frac{\partial\eta}{\partial x}, \tag{12a}$$

$$w(\xi,\eta)=\frac{-1}{\theta}\frac{\partial\theta}{\partial\eta}, \tag{12b}$$

$$p(\xi,\eta)=f(\xi)\eta+g(\xi)d(\xi,\eta)-e(\xi,\eta) \tag{12c}$$

and where

$$f(\xi)=\frac{1}{\rho_e}\frac{\mathrm{d}\rho_e}{\mathrm{d}x}+\frac{1}{u_e}\frac{\mathrm{d}u_e}{\mathrm{d}x}-\frac{1}{2\xi}\frac{\mathrm{d}\xi}{\mathrm{d}x}-j\tan\phi\frac{\mathrm{d}\phi}{\mathrm{d}x}, \tag{12d}$$

$$g(\xi)=j\left[\frac{1}{r_0}\frac{\mathrm{d}r_0}{\mathrm{d}x}+\tan\phi\frac{\mathrm{d}\phi}{\mathrm{d}x}\right] \tag{12e}$$

and

$$\mathrm{d}(\xi,\eta)=\int_0^\eta\frac{1}{t}\mathrm{d}\bar{\eta}, \tag{12f}$$

$$e(\xi,\eta)=\frac{\mathrm{d}\xi}{\mathrm{d}x}\int_0^\eta\frac{1}{\theta}\frac{\partial\theta}{\partial\xi}\mathrm{d}\bar{\eta}. \tag{12g}$$

We relegate the details of the discretization of equation (11) to the Appendix.

In practice, whether by method 1 or method 2, evaluation of η_x occurs along stations of constant ξ. For fixed ξ, the integrals which appear in both methods [for example, in equations (12f, g)] assume the form

$$i(\eta)\equiv\int_0^\eta h(\bar{\eta})\mathrm{d}\bar{\eta}, \tag{13}$$

where h is an arbitrary function of η. It remains to describe their spectrally accurate numerical approximation. For this purpose, let the computational domain $0\leqslant\eta\leqslant\eta_{\mathrm{MAX}}$ be partitioned into N subintervals such that $0=\eta_0<\eta_1<\eta_2<\cdots<\eta_N=\eta_{\mathrm{MAX}}$. At the grid points η_n, we have

$$i(\eta_n)=\sum_{k=0}^{n}\Delta i(\eta_k),\qquad \Delta i(\eta_n)\equiv\begin{cases}0 & (n=0)\\ \displaystyle\int_{\eta_{n-1}}^{\eta_n}h(\bar{\eta})\mathrm{d}\bar{\eta} & (n=1,2,\ldots,N)\end{cases} \tag{14}$$

If $h_n\equiv h(\eta_n)$, and i_n and Δi_n are the discrete approximations of $i(\eta_n)$ and $\Delta i(\eta_n)$, respectively, then the discrete analogue of equation (13) is the following:

$$i_n=\sum_{k=0}^{n}\Delta i_k,\qquad \mathbf{\Delta i}_1=\mathbf{Qh}. \tag{15}$$

In equation (15), $\mathbf{Q}$ is an $N \times (N+1)$ quadrature operator, and, for convenience, the following vector notation has been adopted:

$$\mathbf{h} \equiv \begin{bmatrix} h_0 \\ h_1 \\ \vdots \\ h_N \end{bmatrix}, \qquad \mathbf{h}_1 \equiv \begin{bmatrix} h_1 \\ h_2 \\ \vdots \\ h_N \end{bmatrix}. \tag{16}$$

Conventions similar to equation (16) hold for all other vector quantities.

Equation (15) is general in the sense that $\mathbf{Q}$ can represent any quadrature rule. For example, if the trapezoidal quadrature rule is adopted, then $\mathbf{Q}$ is bidiagonal and $\mathbf{i}$ approximates $i(\eta)$ to second-order accuracy. For the hydrodynamic stability applications which motivate this work, we are interested in attaining highly accurate and smooth solutions. Accordingly, we specialize $\mathbf{Q}$ to a collocation method based on Chebyshev polynomial approximation, for which $\mathbf{Q}$ is a dense matrix and for which spectral accuracy is attained. The collocation method applied here to the extraction of the wall-normal velocity is adapted from the method described in Reference 2 for solution of the compressible boundary-layer equations, to which the reader is referred for greater detail.

In brief, we approximate continuous non-periodic function $h(\tilde{\eta})$ on $[-1, 1]$ by a finite series expansion $h_N(\tilde{\eta})$ in an orthogonal basis set of Chebyshev polynomials $T_n(\tilde{\eta})$, namely

$$h_N(\tilde{\eta}) = \sum_{n=0}^{N} \hat{h}_n T_n(\tilde{\eta}), \tag{17a}$$

$$T_n(\tilde{\eta}) = \cos[n \cos^{-1} \tilde{\eta}], \tag{17b}$$

where coefficients $\hat{h}_n$ are termed the 'spectrum' of $h_N(\tilde{\eta})$. Using the 'natural' Gauss–Lobatto set of collocation points

$$\tilde{\eta}_n = \cos z_n, \qquad z_n = \frac{\pi n}{N} \quad (n = 0, 1, 2, \ldots, N), \tag{18}$$

we obtain from equation (17) the discrete Fourier cosine transform

$$h_n \equiv h_N(\tilde{\eta}_n) = \sum_{k=0}^{N} \hat{h}_k \cos \frac{n\pi k}{N}. \tag{19}$$

The corresponding discrete inverse transform gives the spectrum $\hat{h}_n$, namely

$$\hat{h}_n = \frac{2}{N c_n} \sum_{k=0}^{N} \frac{\hat{h}_k}{c_k} \cos \frac{n\pi k}{N}, \tag{20a}$$

where

$$c_k = \begin{cases} 2, & k = 0 \text{ or } k = N \\ 1, & 0 < k < N. \end{cases} \tag{20b}$$

It is convenient to express equation (20) as a matrix–vector operation

$$\hat{\mathbf{h}} = \mathbf{P}_N \mathbf{h}, \tag{21}$$

where $\mathbf{P}_N$ is a dense $(N+1) \times (N+1)$ matrix whose elements are available by inspection from equations (20).

Interpreted in the light of transform pair (19) and (20), equations (17) define the spectral interpolation polynomial, exact, by definition, at the collocation points. Unlike polynomial interpolating series defined on equally spaced intervals, series (17) converges uniformly to $h(\tilde{\eta})$ as $N \to \infty$. Moreover, it can be shown that, for continuously differentiable functions h, coefficients $\hat{h}_n$ decay to zero faster than any finite power of $1/N$ as $N \to \infty$. This is termed 'spectral convergence'.

Now, to form quadrature operator $\mathbf{Q}$, we consider

$$\int_{\tilde{\eta}_{n-1}}^{\tilde{\eta}_n} h(\tilde{\eta})\,\mathrm{d}\tilde{\eta} \cong E_n \equiv \int_{\tilde{\eta}_{n-1}}^{\tilde{\eta}_n} h_N(\tilde{\eta})\,\mathrm{d}\tilde{\eta} = \int_{\tilde{\eta}_{n-1}}^{\tilde{\eta}_n} \sum_{k=0}^{N} \hat{h}_k T_k(\tilde{\eta})\,\mathrm{d}\tilde{\eta} = \sum_{k=0}^{N} \hat{h}_k \int_{\tilde{\eta}_{n-1}}^{\tilde{\eta}_n} T_k(\tilde{\eta})\mathrm{d}\tilde{\eta}. \tag{22}$$

In matrix–vector form, equation (22) becomes

$$\mathbf{E}_1 = \mathbf{R}_N \mathbf{h}, \tag{23}$$

where $\mathbf{E}_1$ is an N-vector and $\mathbf{R}_N$ is a dense $N \times (N+1)$ matrix whose elements are obtained from equation (22) with the help of equations (17) and (18) as follows:

$$R_{kn} = -\int_{z_{k-1}}^{z_k} \sin z \cos(nz)\mathrm{d}z \quad (k = 1, 2, \ldots, N, \quad n = 0, 1, 2, \ldots, N). \tag{24}$$

From equations (21) and (23), the $N \times (N+1)$ spectral quadrature operator $\mathbf{Q}$ is defined as

$$\mathbf{Q} = \mathbf{R}_N \mathbf{P}_N. \tag{25}$$

Finally, we note that a continuous mapping $\eta = \eta(\tilde{\eta})$ is necessary to take the natural Chebyshev domain $-1 \leqslant \tilde{\eta} \leqslant 1$ onto the computational domain $0 \leqslant \eta \leqslant \eta_{\mathrm{MAX}}$. Such a mapping is also useful to redistribute collocation points, clustering them in regions of high gradients. In practice, the metric $\mathrm{d}\tilde{\eta}/\mathrm{d}\eta$, computed either analytically, or numerically to spectral accuracy, is incorporated directly into quadrature operator $\mathbf{Q}$.

We close by summarizing briefly the complete algorithm for extracting wall-normal velocity, as integrated into the spectrally accurate boundary-layer code of Pruett and Streett.[2] Following Reference 2, governing Equations (1) are solved for discrete marching steps $\xi_0 < \xi_1 < \xi_2 < \cdots$, each corresponding to a unique streamwise station. Immediately available from the converged boundary-layer solution at each fixed ξ are the quantities $\theta, \theta_\xi, \theta_\eta$ and t which appear in the integrands of equations (5a), (8) and (12). These integrals are evaluated numerically to spectral accuracy following the quadrature procedure of equations (13)–(25). In the discrete approximation, these integrals are vector quantities. Also needed at each discrete ξ are certain scalar quantities: for example, $f(\xi)$ and $g(\xi)$ in equations (12) of method 2, or the coefficient of $y_{2\mathrm{D}}$ in equation (8) of method 1. These are readily evaluated from the discrete edge and geometry data $\tau[x(\xi)]$, where $\tau \in (\rho_e, u_e, \mu_e, r_0, \phi)$. Currently, we use cubic splines for smooth interpolation of τ as well as for computation of derivatives of the form $\mathrm{d}\tau/\mathrm{d}x$. Following the evaluation of all necessary scalar and vector quantities at fixed ξ, the discrete approximation of η_x is obtained from either method 1 or method 2. Wall-normal velocity is obtained subsequently from equation (4) and the boundary-layer solution (V, F, θ). Despite the awkward nature of the expressions which comprise methods 1 and 2, their evaluation is straightforward, is computationally efficient and involves only the numerical machinery already in place for the solution of boundary-layer equations (1).

4. CODE VALIDATION

Our purpose here is to offer reasonable validation of the present method. To obtain the results of this section, we solve equations (1) by the fully implicit method of Pruett and Streett,[2] which has been modified to incorporate the Levy–Lees transformation (2). We exploit second-order backward differencing in the time-like dimension, although the method allows up to fifth-order differencing. For convenience, the marching scheme uses equally spaced steps in physical space. A further modification permits the option of either preconditioned Richardson iteration or Newton iteration within each implicit marching step. Typically, we iterate using the Richardson scheme until the discrete residual is small enough so that one final (computationally intensive) Newton iteration achieves 'full' convergence. Following convergence of the iteration, the wall-normal velocity is extracted by the spectral collocation method presented herein. All computations assume that the wall is adiabatic, although the boundary-layer code permits fixed-temperature wall conditions as well. The following transformation has been used to map from the Chebyshev domain $\tilde{\eta}\in[-1, 1]$ to the computational domain $\eta\in[0, \eta_{MAX}]$, as discussed in the previous section:

$$\eta(\tilde{\eta})=\frac{0{\cdot}5\eta_{MAX}[1-\tanh(\sigma)](1-\tilde{\eta})}{1-\tanh[0{\cdot}5\sigma(1-\tilde{\eta})]}. \tag{26}$$

In equation (26), σ is a free parameter which controls the strength of stretching. The results shown use $\eta_{MAX}=21$ and $\sigma=0{\cdot}7$, chosen after some numerical experimentation. For a well-resolved grid, the solution is not particularly sensitive to the choice of σ. However, it is important that η_{MAX} be sufficiently large so that the far-field boundary condition does not 'pinch' the boundary-layer flow. Our experience is that η_{MAX} should be chosen so that $y(\eta_{MAX})$ is 2 to 3 boundary-layer displacement thicknesses from the wall.

We take the flow parameters and the geometry of the validation case from the high-speed ($M_\infty=8{\cdot}0$) wind-tunel experiment of Stetson *et al.*[13] on a sharp cone at zero angle of incidence. These are

$$\phi=7^\circ, \qquad M_e=6{\cdot}8, \qquad T_e^*=128^\circ\,\mathrm{R}, \qquad Re_1=1.4\bar{3}\times10^6\,\mathrm{ft}^{-1} \tag{27}$$

where Re_1 is the unit Reynolds number based on edge conditions. Except quite near the tip, the flow on a sharp cone exhibits conditions at the boundary-layer edge which are approximately constant. Accordingly, we assume that the edge values remain constant in x, and we set reference values equal to their respective edge values, e.g. $u_r^*=u_e^*$. We note, however, that both methods for extracting v have been validated for the fully general case in which both the geometry and edge data vary with x.

Figure 2 compares the wall-normal velocity obtained by the present method with that of a second-order finite-difference method. The parameter values are those given in equation (27), and the comparison is made at $x^*=2{\cdot}0$ ft. To obtain the finite-difference results, we solve the boundary-layer equations using the time-honoured method of Harris and Blanchard.[1] Document[1] describing their code, however, does not discuss extraction of the wall-normal velocity, and in their baseline code, v is accurate only to first order,[11] inadequate for our purposes here. Recently, Chang[14] has modified their algorithm independently to obtain the v-velocity to second-order accuracy. The 'finite-difference' results presented in Figure 2 were obtained using Chang's method, with 102 points in the wall-normal direction and an extremely small marching step size of $\Delta x^*=0{\cdot}005$ ft. For clarity, only every fourth point is plotted. The spectral results shown for comparison were obtained using the same Δx but only 42 points in η, sufficient for 'engineering' accuracy. The results are virtually indistinguishable.

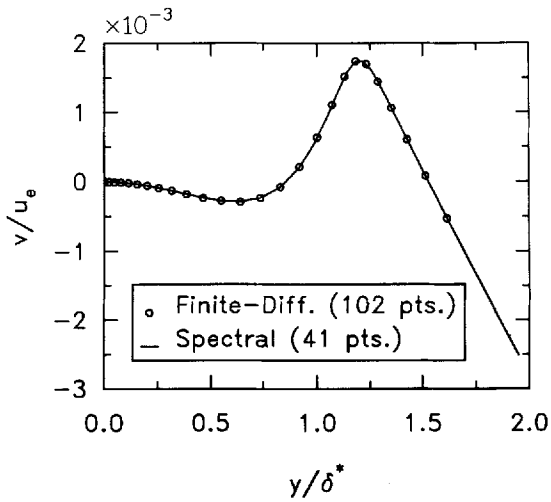

Figure 2. Comparison of spectral and second-order finite-difference methods for the wall-normal velocity at $x^* = 2{\cdot}0$ ft

Because the smoothness of the velocity profiles is of prime concern, all results to follow were obtained using 102 ($N = 101$) collocation points in the wall-normal η direction, far more than the 40 or so necessary to obtain 3-digit engineering accuracy. In fact, as will be shown, at this high resolution, velocity and temperature distributions at fixed ξ are smooth to 13 digits. Furthermore, for the results to follow, we have used a much higher increment of $\Delta x^* = 0{\cdot}1$ ft in the marching direction, sufficient for validation studies.

Since the boundary-layer equations are derived by neglecting certain terms of the Navier Stokes equations, it is of some interest to compare present results with schemes based on approximations which are 'closer' to Navier–Stokes. Figure 3 compares the radial velocity obtained by the present method with the results of a parabolized Navier–Stokes (PNS) calculation using the wall-tested code of Korte.[15] The PNS code exploits finite-difference techniques and is of second-order accuracy in both the marching (axial) s and cross-stream (radial) r directions. The velocities (u', v') computed by the PNS code are in cartesian co-ordinates, and for comparison, the results of the boundary-layer calculation are transformed accordingly. The PNS scheme is fully explicit and the marching step size is the maximum allowed by stability (CFL) considerations. The PNS computation uses 150 grid points in the radial dimension, approximately 30 of which lie within the boundary layer. At this resolution, the PNS calculation is fairly severely underresolved in the radial direction as indicated by the clearly visible grid-scale oscillation. (According to Reference 1, approximately 200 points are necessary using second-order finite-difference methods to resolve the boundary-layer region sufficiently to capture the temperature gradient at the wall to 0·1% error.) Unfortunately, it is impractical for existing computer resources to pack significantly more points within the boundary layer since, in the fully explicit PNS code, the marching step size decreases as $\Delta r_{\mathrm{MIN}}^2$, where Δr_{MIN} is the minimum grid interval in the radial dimension. Similar computational barriers were encountered when attempting to compare the present method against a compressible Navier–Stokes (NS) calculation using the finite-volume code of Jacobs,[16] for which it was impractical to resolve the flow to the degree desired. Despite these difficulties, the radial velocities obtained from the PNS and boundary-layer (BL) computations, which are compared at $s = 3{\cdot}28$ ft (1 m) in Figure 3, are in reasonable agreement. The maximum velocity, the boundary-layer edge location and the far-field decay of v'

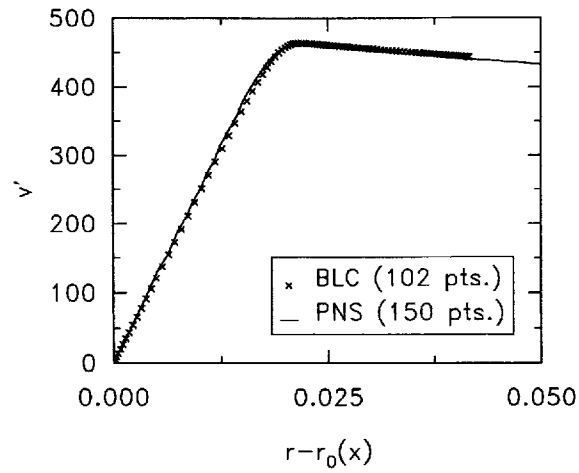

Figure 3. Radial velocity at $s^* = 3{\cdot}28$ ft (1 m)

all agree well. We also note that the shock obliqueness angle derived by the PNS calculation is about 11°, for which the corresponding post-shock Mach number is 6·8, in concurrence with the experimental results of Stetson *et al.*[13] and the edge Mach number used for the BL calculation. We further mention that the (underresolved) NS[16] and PNS[15] calculations are in close agreement.

The present method has been further validated by Kopriva,[17] who has employed the spectral-collocation BL code to check recent adaptations of his spectral multidomain code (inviscid) to incorporate the viscous terms of the CNSE. Agreement between Kopriva's moderately resolved NS computations and the present method is quite good for test cases which include Mach 2 flow along a circular cylinder and Mach 2·2 flow over a flat plate.

The previous checks against existing codes assure us that there are no grievous errors in the current method of extracting wall-normal velocity. We now turn to self-consistency checks. One motivation for developing independent methods for evaluating η_x is to provide a check otherwise unavailable. For the same test case as before, with parameter values given in equations (27), Figure 4 compares η_x at $x^* = 2{\cdot}0$ ft as computed by methods 1 and 2. These results appear virtually identical in Figure 4, and, in fact, they agree to at least 11 significant digits at every gridpoint.

As mentioned in Section 1, the current method also leaves the continuity equation available as a check on the quality of the discrete solution. For this purpose, it is preferable to expand the continuity equation in terms of the physical co-ordinates, whereby we obtain the following expression, valid for flat plate, hollow cylinder and cone geometry:

$$\frac{\partial(\rho u)}{\partial x} + \frac{\partial(\rho v)}{\partial y} + j\frac{\rho u \sin\phi}{r} + j\frac{\rho v \cos\phi}{r} = 0. \tag{28}$$

Figure 5 presents the discrete residual of equation (28) at $x^* = 3{\cdot}0$ ft along the cone, computed by summing the four terms on the left-hand side. Again, the parameter values are those given in equations (27). Derivatives are evaluated in computational space by the appropriate chain rules, thereby avoiding interpolation in physical space. The continuity equation is satisfied to approximately 11 orders of magnitude. That there remains considerable structure in the wall-normal

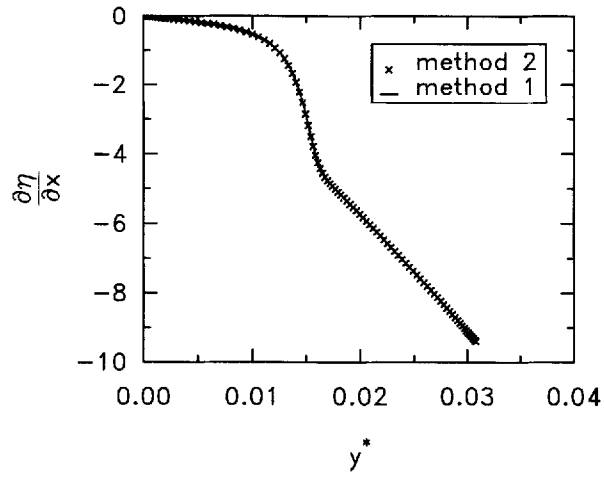

Figure 4. Comparison of alternative derivations of $\partial\eta/\partial x$ at $x^* = 2{\cdot}0$ ft

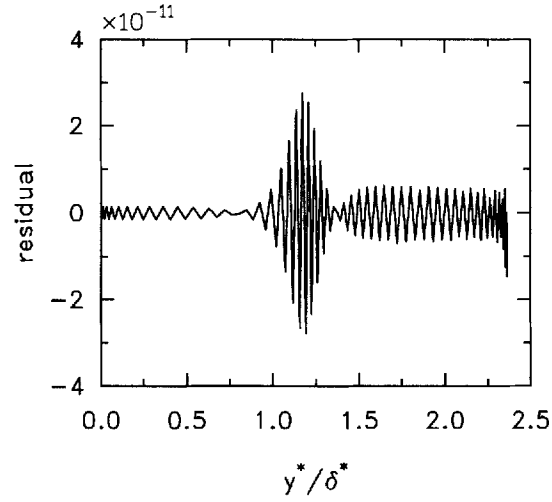

Figure 5. Residual of the continuity equation

distribution of the residuals suggests that, with further tuning of σ and N, one could likely drive the residual at least another order of magnitude toward machine zero (10^{-14}).

One final measure of the quality of the spectral numerical method is the decay of the spectra [refer to equation (20a)] as shown at station $x^* = 3{\cdot}0$ ft along the cone in Figure 6. The decay of the temperature, u-velocity and v-velocity spectra each by at least 13 orders of magnitude implies that the solution is smooth to nearly the full 14-digit precision of the (Cray 2) machine. The linear decay rate on the logarithmic scale is indicative of 'spectral convergence', by which we mean that truncation error decays faster than any finite power of $1/N$ as $N \to \infty$.

Our interest in an accurate and smooth solution is not just academic. Analyses of stability based on parallel linear stability theory result in eigenvalue problems which require first and

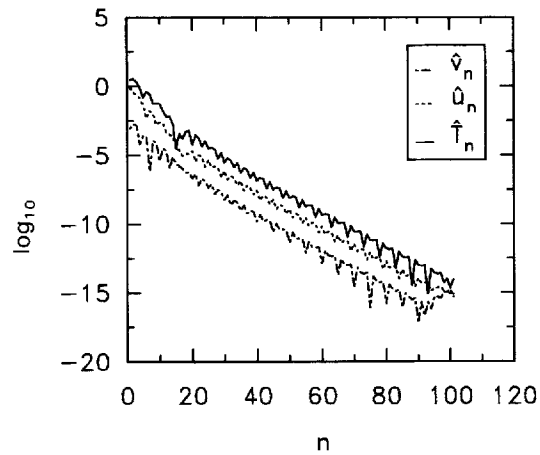

Figure 6. Decay of the Chebyshev spectra

second partial derivatives with respect to y of both the mean u-velocity and the mean temperature. In addition, analyses based on non-parallel theory require the mean v-velocity and its derivatives as well. For $N = 101$, each spectrally accurate numerical differentiation of the boundary-layer solution results in a loss of significance of 2 to 3 digits due to the unavoidable magnification of round-off errors. Yet because of the initially high quality of the solution, we obtain first and second derivatives which are smooth to at least 10 and 7 digits, respectively.

Finally, we comment briefly on computational efficiency. For $N = 101$, the spectral collocation method of Pruett and Streett[2] modified for the Levy–Lees transformation (2) requires slightly less than one CPU second per marching step on a Cray 2 supercomputer to solve boundary-layer equations (1). Of this second, extraction of the wall-normal velocity by method 2 consumes a small percentage, whereas the computational requirements of method 1 are virtually negligible. It was originally thought that the integral equation method (method 2) might enjoy some advantages in the distribution of error. However, from the data for Figure 4, it appears that any such advantage is insignificant.

5. APPLICATION

We now turn to an application of the method to a problem of both long-standing and immediate interest which concerns the stability characteristics of the boundary layers of cylinders and cones relative to those of the more commonly studied flat plate. While it is beyond the scope of this paper to address stability theory *per se*, some light is shed on stability issues by comparing boundary-layer 'profiles' for the flat plate, the hollow cylinder and the cone.

Here, we consider the same flow parameters and cone geometry given in equations (27). Presented for comparison, the hollow cylinder can be regarded as the axisymmetric equivalent of the flat plate (that is, the boundary layer is assumed to have no thickness at the sharp leading edge). The radius of the cylinder is taken to be $r_0^* = 0{\cdot}3684$ ft, equivalent to that of the cone at station $x^* = 3{\cdot}0$ ft. For reference, Figure 7 compares the growth of the three boundary layers in terms of displacement thickness δ^* as defined below:[3]

$$\delta^*\left[1+\frac{\delta^*}{2r_0^*}\right]^j = \int_0^\infty \left[\frac{r^*}{r_0^*}\right]^j \left[1-\frac{\rho^* u^*}{\rho_e^* u_e^*}\right] \mathrm{d}y^*. \tag{29}$$

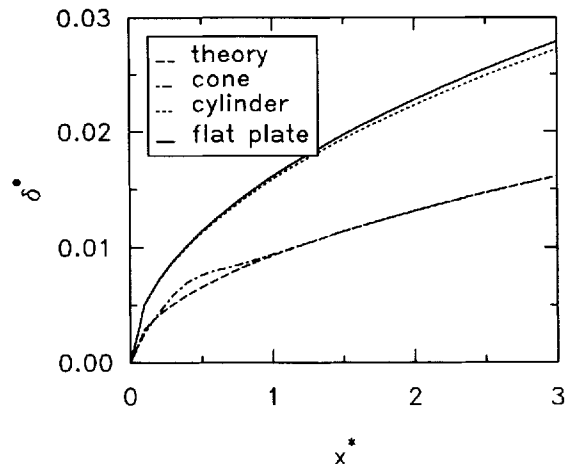

Figure 7. Streamwise evolution of boundary-layer displacement thickness

As is well-known, the self-similar boundary layer on the flat plate grows proportionately to $\sqrt{x^*}$. On the other hand, the boundary layer along the cylinder is non-similar because the 'curvature' K, quantified by the ratio $K = \delta^*/r_0^*$, increases in the streamwise direction due to the growth of δ^*. Provided $K \ll 1$, as is the case here, the displacement thickness on the cylinder exhibits growth much like that of the flat plate. Also as is well-known, the boundary layer on the cone asymptotes to a growth rate $1/\sqrt{3}$ times that of the flat plate, as predicted by the Mangler transformation.[18] Mangler's theory ignores transverse curvature and is invalid near the sharp tip of the cone, where K is large. As noted by Malik and Spall,[19] the curvature K along the cone decreases in the streamwise direction, in contrast to its increase along the cylinder. As they also note, the effect on stability of the disparity in scales is that the boundary layer on the cone supports higher disturbance frequencies.

Figure 8(a)–(c) compares, respectively, the temperature, streamwise velocity and wall-normal velocity distributions of the cone, cylinder and flat-plate boundary layers at $x^* = 3{\cdot}0$ ft. When the wall-normal co-ordinate y^* is scaled by the appropriate displacement thickness, the temperature and stream-wise velocity distributions of the flat plate, hollow cylinder and cone 'collapse' and are virtually coincident. There is a slight effect due to transverse curvature which tends to produce a slightly 'fuller' u-velocity profile and a 'thinner' temperature profile with increasing K. For the parameter values of the test case, the curvature K values at $x^* = 3{\cdot}0$ ft are 0·0, 0·0744 and 0·0440, for the flat plate, cylinder and cone, respectively. Our principle interest lies in comparison of the wall-normal velocities. Whereas the v-velocity in the flat-plate boundary layer is constant at the edge, that of the cylinder decays like $1/r$ in the far field. Otherwise, they are qualitatively similar. In contrast to the hollow cylinder and flat plate, the cone has v-velocity which changes sign, is negative for large y, and has a large, nearly constant gradient in the far field. For comparison, Figure 8(c) also shows the inviscid solution for the wall-normal velocity, obtained from the code of Marconi and co-workers.[20] Note that the far-field boundary-layer solution and the inviscid solution have similar trends as anticipated, lending additional confidence in the method.

To highlight the influence of the differences in wall-normal velocity which are due to geometry, it is useful to examine the individual contributions of each of the four terms to the left-hand side of continuity equation (28), as shown in Figure 9. For the flat plate [Figure 9(a)], the third and fourth terms vanish, and the first and second terms exactly balance. For the cylinder [Figure

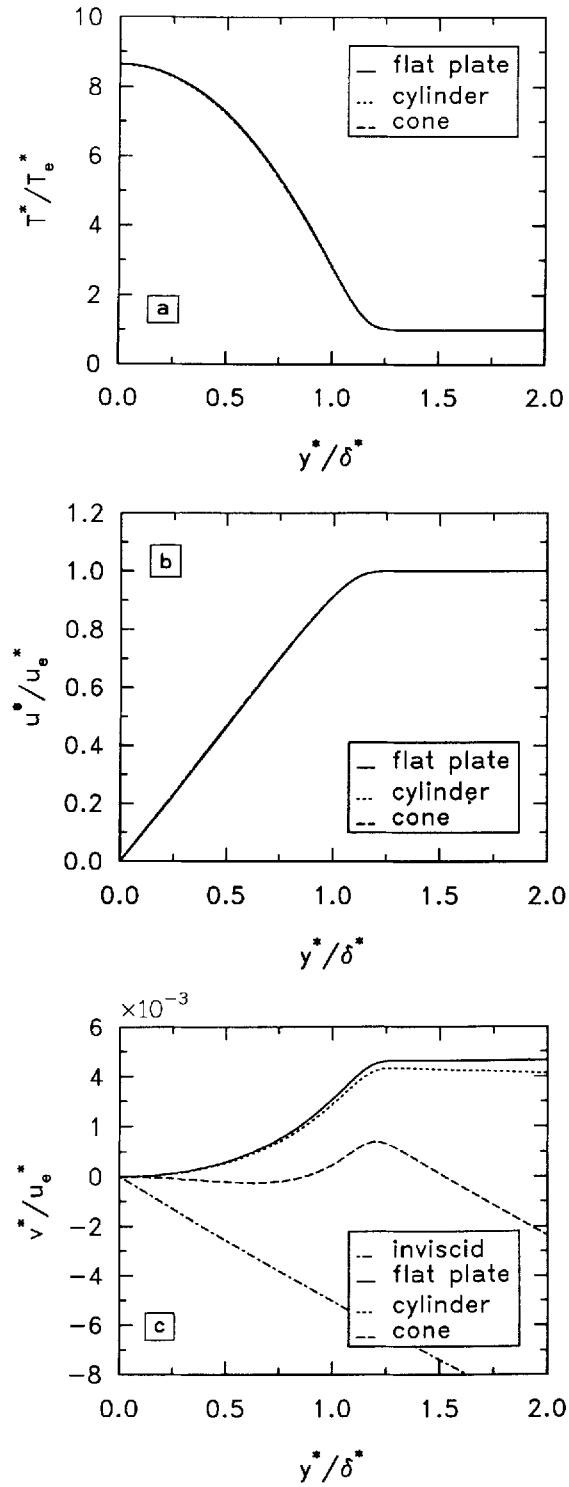

Figure 8. Temperature (a) streamwise velocity (b) and wall-normal velocity (c) distributions at $x^* = 3{\cdot}0$ ft

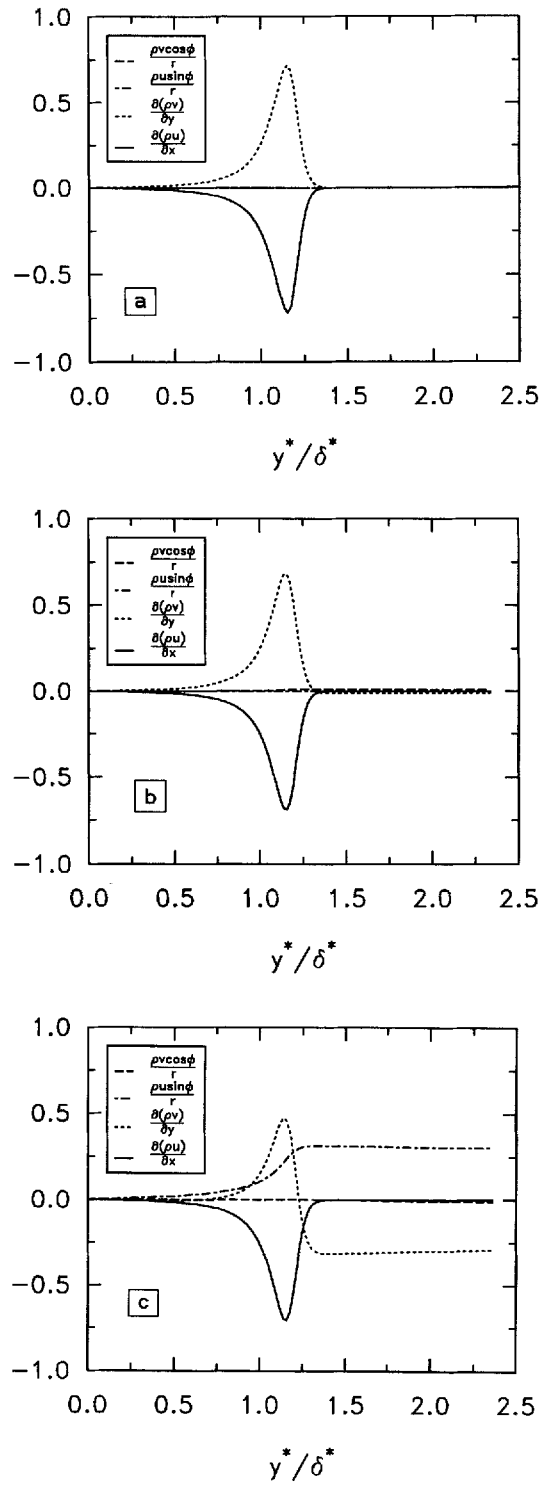

Figure 9. Terms of the continuity equation compared at station $x^* = 3{\cdot}0$: (a) flat plate; (b) cylinder; and (c) cone

9(b)], there is a small non-zero contribution from the fourth term, but the overall picture closely resembles that of the flat plate. In contrast, for the cone [Figure 9(c)], terms 1 and 2 approximately balance in the near-wall region. However, the third term contains a large contribution in the far field which is offset approximately by the far-field contribution of the second term.

Figure 9(c) has implications for classical linear stability theory, in which the parallel-flow approximation plays an important role. In theory, the parallel-flow approximation arises from the recognition that the wall-layer mean flow evolves slowly in x relative to the scale of a typical disturbance wavelength, in which case certain terms in the linearized disturbance equations are 'small' and can reasonably be neglected. In practice (i.e. in stability codes), however, the parallel-flow approximation is typically implemented by requiring of the mean flow that

$$v=0 \quad \text{and} \quad \frac{\partial}{\partial x}=0. \tag{30}$$

Condition (30) is self-consistent for the boundary-layer flow along a flat plate or a hollow cylinder in the sense that a parallel mean flow can simultaneously satisfy continuity equation (28) and approximation (30). From Figure 9(c), however, we find that equations (28) and (30) are inconsistent for the cone, since the term $\rho u \sin \phi/r$ does not vanish under approximation (30). Violation of the continuity equation by the assumption of parallelism in particularly noxious since it leads to inconsistency between the conservative and non-conservative formulations of the linearized disturbance equations.[21] In fact, Pruett *et al.*[21] have shown rigorously that there is no self-consistent parallel-flow approximation for the stability of the flow along a cone. If the stability of a conical flow is properly treated only by methods which allow non-parallelism, then the wall-normal velocity assumes importance. Consequently, the care which has been devoted here to securing an accurate and smooth determination of v is not ill-spent.

6. CONCLUSIONS

The fully implicit, spectral collocation method developed by Pruett and Streett[2] for solution of the compressible boundary-layer equations has been extended to incorporate the Levy–Lees[3] transformation and spectrally accurate evaluation of the wall-normal velocity. The Levy-Lees transformation is essential to the stability of the numerical method for certain classes of compressible boundary-layer flows; however, it renders determination of the wall-normal (v) velocity non-trivial. Two methods of determining v are presented and are shown to be numerically equivalent. The generalized algorithm is valid for non-similar, two-dimensional or axisymmetric laminar boundary-layer flows with varying edge conditions. Computation on a highly resolved mesh results in a discrete solution which satisfies the continuity equation nearly to machine precision, while requiring only about 1 s of CPU time per marching step on a Cray 2 supercomputer. Because of its generality, and the accuracy and smoothness of the discrete solution, the present method is well-suited to providing the mean-flow velocity and temperature distributions needed for analyses of the stability of compressible boundary-layer flows, whether by classical linear stability theory or by recent methods which treat non-parallelism of the mean flow. Since mean-flow non-parallelism can significantly affect the stability of high-speed, wall-bounded flow,[5] the contribution of wall-normal velocity should not be cavalierly disregarded.

ACKNOWLEDGEMENTS

The author is indebted to Drs. Julius Harris and Craig Streett for many helpful discussions and considerable insight. The assistance to Drs. Chau-Lyan Chang, John Korte, Peter Jacobs and David Kopriva in validating results is also gratefully acknowledged.

APPENDIX

For completeness, we describe briefly a solution procedure for the discrete analogue of integral equation (11). For fixed ξ, equation (11) has the form

$$q(\eta)=\int_0^{\eta} w(\eta)q(\eta)\,\mathrm{d}\eta+p(\eta). \tag{31}$$

Note, by inspection of equation (12a), $q(0)=0$. From (31) we obtain

$$q(\eta_n)-q(\eta_{n-1})=\int_{\eta_{n-1}}^{\eta_n} w(\eta)q(\eta)\,\mathrm{d}\eta+(p_n-p_{n-1}) \quad (n=1, 2, 3, \ldots, N). \tag{32}$$

Following the notations regarding equations (14)–(16), the discrete approximation of equation (32) is

$$\mathbf{M}\mathbf{q}_1=\mathbf{Q}_1\mathbf{W}\mathbf{q}_1+\Delta\mathbf{p}_1, \tag{33}$$

where $\mathbf{W}$ is the $N\times N$ diagonal 'weighting' matrix

$$\mathbf{W}=\begin{bmatrix} w_1 & & & \\ & w_2 & & \\ & & \ddots & \\ & & & w_N \end{bmatrix}, \tag{34}$$

$\mathbf{M}$ is the $N\times N$ bidiagonal matrix

$$\mathbf{M}=\begin{bmatrix} 1 & & & & & \\ -1 & 1 & & & & \\ & -1 & 1 & & & \\ & & & \cdot & & \\ & & & & \cdot & \\ & & & & & \cdot \\ & & & & -1 & 1 \end{bmatrix}, \tag{35}$$

$\mathbf{Q}_1$ is the $N\times N$ matrix formed by eliminating the first column of the $N\times(N+1)$ numerical quadrature operator $\mathbf{Q}$ [refer to equation (25)], and $\Delta\mathbf{p}_1$ is the N-vector whose components are $\Delta p_n=p_n-p_{n-1}$ $(n=1, 2, 3, \ldots, N)$. Simplifying (33), we obtain $\mathbf{q}_1$ as the solution to the Nth-order linear system

$$\mathbf{A}\mathbf{q}_1=\Delta\mathbf{p}_1, \quad \text{where} \quad \mathbf{A}\equiv\mathbf{M}-\mathbf{Q}_1\mathbf{W}. \tag{36}$$

REFERENCES

1. J. E. Harris and D. K. Blanchard, 'Computer program for solving laminar, transitional, or turbulent compressible boundary-layer equations for two-dimensional and axisymmetric flow', *NASA TM-83207*, 1982.
2. C. D. Pruett and C. L. Streett, 'A spectral collocation method for compressible, nonsimilar boundary layers', *Int. j. numer. methods fluids*, **13**, 713–737 (1991).
3. F. M. White, *Viscous Fluid Flow*, McGraw-Hill, New York, 1974.
4. P. W. Duck, 'The inviscid axisymmetric stability of the supersonic flow along a cylinder', *J. Fluid Mech.*, **214**, 611–637 (1990).
5. N. M. El-Hady, 'Nonparallel instability of supersonic and hypersonic boundary layers', *AIAA Paper No. 91-0324*, 1991.
6. A. Thumm, W. Wolz and H. Fasel, 'Numerical simulation of spatially growing three-dimensional disturbance waves in compressible boundary layers', in D. Arnal and R. Michel (eds), *Laminar-Turbulent Transition: IUTAM Symposium, Toulouse, France, 1989*, Springer, Berlin, 1990, pp. 303–308.

7. N. M. El-Hady, 'Spatial three-dimensional secondary instability of compressible boundary-layer flows', *AIAA J.*, **29,** 688–696 1991.
8. P. Balakumar and M. R. Malik, 'Waves produced from a harmonic point source in a supersonic boundary layer', *AIAA Paper No. 91-1646*, 1991.
9. F. P. Bertolotti, 'Linear and nonlinear stability of boundary-layers with streamwise varying properties', *Ph.D. Thesis*, Ohio State University, 1990.
10. C.-L. Chang, M. R. Malik, G. Erlebacher and M. Y. Hussaini, 'Compressible stability of growing boundary layers using parabolized stability equations', *AIAA Paper No. 91-1636*, 1991.
11. J. E. Harris, personal communication, 1991.
12. C. D. Pruett, 'On the wall-normal velocity of the compressible boundary-layer equations', *NASA Contract Report 4419*, 1991.
13. K. F. Stetson, E. R. Thompson, J. C. Donaldson and L. G. Siler, 'Laminar boundary-layer stability experiments on a cone at mach 8. Part 1: Sharp Cone', *AIAA Paper No. 83-1761*, 1983.
14. C.-L. Chang, High-Technology Corp., Hampton, Virginia 23666, personal communication, 1992.
15. J. J. Korte, 'An explict upwind algorithm for solving the parabolized Navier–Stokes equations', *NASA TP-3050*, 1991.
16. P. A. Jacobs, 'Single-block Navier-Stokes integrator', *ICASE Interim Report 18 (NASA Contractor Report 18713)*, 1991.
17. D. A. Kopriva, 'Spectral solution of the viscous blunt body problem,' *FSU-SCRI-92-68*, Florida State University, Supercomputer Computations Research Institute, Tallahassee, Florida, 1992.
18. W. Mangler, 'Zusammenhang zwischen Ebenen und Rotationssymmetrischen Grenzschichten in Kompressiblen Fluessigkeiten', *Z. Angew Math. Mech.*, **28,** 97–103 (1948).
19. M. R. Malik and R. E. Spall. 'On the stability of compressible flow past axisymmetric bodies', *J. Fluid Mech.*, **228,** 443–463 (1991).
20. F. Marconi, M. Salas and L. Yeager, 'Development of a computer code for calculating the steady super/hypersonic flow around real configurations: vol. I– Computational technique', *NASA CR-2675*, 1976.
21. C. D. Pruett, L. L. Ng and G. Erlebacher, 'On the non-uniqueness of the parallel-flow approximation', in M. Y. Hussaini, A. Kumar and C. L. Streett (eds), *Instability, Transition, and Turbulence*, Springer-Verlag, New York, 1992, pp. 344–355.